Supplementary Information

Table S1. Calculated equilibrium lattice constant (a, Å), bond length of Fe-I (l_{Fe-I}, Å), angle of the I-Fe-I ($\angle\alpha$, °), magnetic moment of Fe (M, μ_B), cohesive energy (E_{coh}, eV/atom), and exchange energy with DFT+U and HSE functional, respectively (E_{exc}= E_{AFM} - E_{FM}, meV).

	a	l_{Fe-I}	$\angle\alpha$	M	E_{coh}	E_{exc} (DFT+U)	E_{exc} (HSE)
Fe_2I_2	3.81	2.68	90.34	~3	3.01	516	478

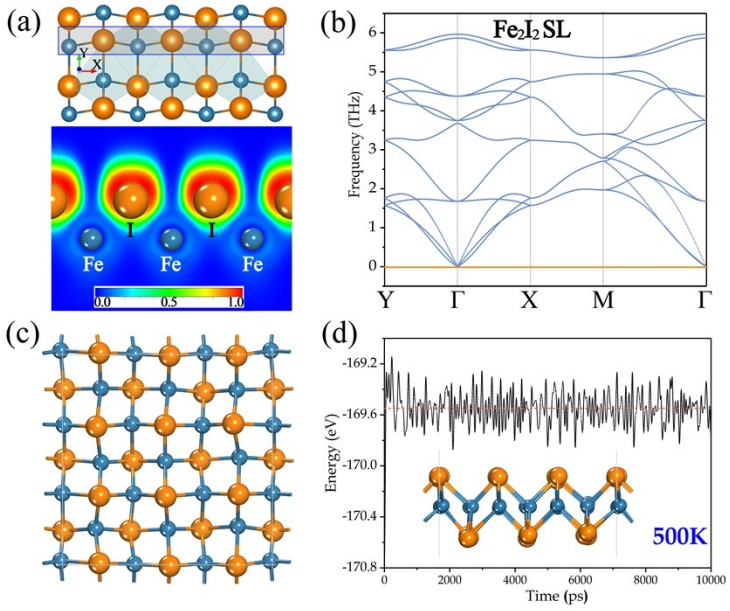

Figure S1. (a) Electron localization function (ELF); ELF = 1.0 (red) and 0.0 (blue) indicate accumulated and vanishing electron density, respectively. (b) Harmonic phonon analysis of SL Fe_2I_2. (c) Snapshot of SL Fe_2I_2 at the end of MD simulation at 500 K after 10 ps. (d) Changes of the total energy with the trajectory time, obtained from MD simulations of SL Fe_2I_2 at 500 K.

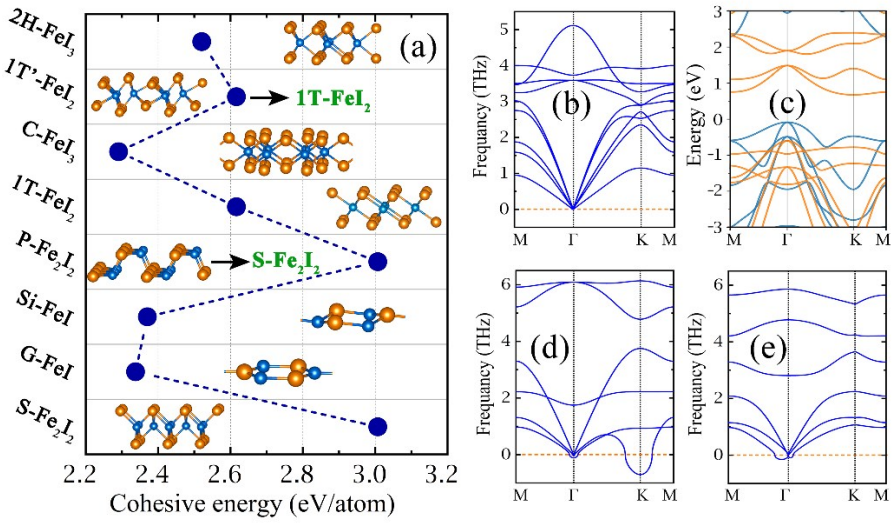

Figure S2. (a) Calculated cohesive energy (E_{coh}, eV/atom) for a wide range of 2D Fe_xI_y binary materials where the insets show their corresponding crystal structures. The 1T'-FeI_2 and P-Fe_2I_2 structures, denoted by the horizontal black arrows, undergo structural phase transitions to the 1T-FeI_2 and S-Fe_2I_2 structures, respectively, after geometry relaxation. (b) Calculated phonon dispersion curves of the proposed 2H-FeI_2. (c) Minority (Orange line) and majority (blue line) spin-resolved band structure of the 2H-FeI_2 layer. (d) and (e) Phonon dispersion curves of the proposed G-FeI, and Si-FeI layers, respectively.

In order to determine the ground state of the 2D Fe_xI_y binary materials, we have constructed seven additional possible configurations based on the conventional prototypes of 2D material family. As shown in Figure S2, these additional 2D Fe_xI_y crystals include the graphene-like FeI (denoted as G-FeI), silicene-like FeI (Si-FeI), phosphorene-like FeI (P-Fe_2I_2), 1T-MoS_2-like FeI_2 (1T-FeI_2), CrI_3-like FeI_3 (C-FeI_3), 1T'-WTe_2-like FeI_2 (1T'-FeI_2), and 2H-MoS_2-like FeI_2 (2H-FeI_2). Overall, the calculations reveal several important results: (1) the square Fe_2I_2 single-layer (SL) (shown in this work, denoted as S-Fe_2I_2) is indeed the ground state with the highest E_{coh}. (2) Similar to the reported 1T-FeI_2 [1-3], the 2H-FeI_2 SL shows an insulating electronic behavior and in-plane

magnetic orientation (MCA = -1.98 meV) with a dynamically stable crystal structure. (3) The 2D G-FeI and Si-FeI hexagonal structures are not stable because of the emergence of imaginary frequencies in the phonon spectra.

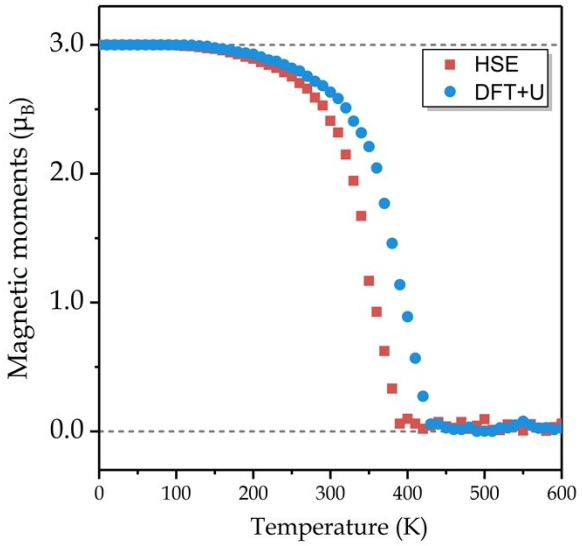

Figure S3. The magnetic moments variation of the Fe atom as functions of temperature by means of Monte Carlo simulations on the basis of 2D Heisenberg Hamiltonian model.

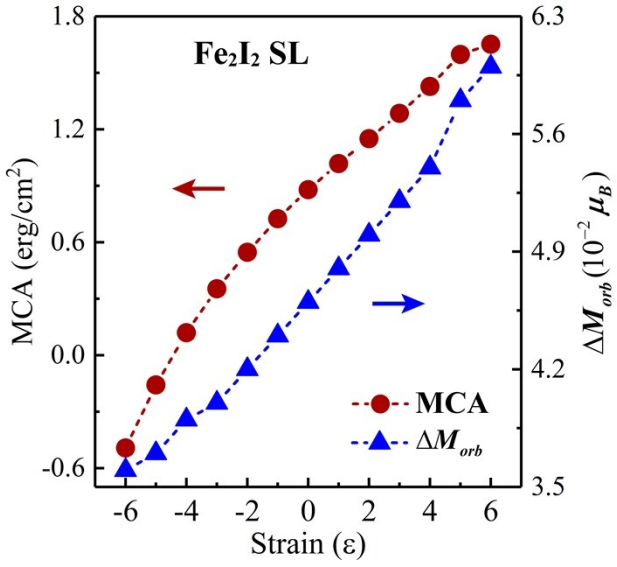

Figure S4. The variation of MCA and orbital moment anisotropy verse strain effect for Fe_2I_2 SL.

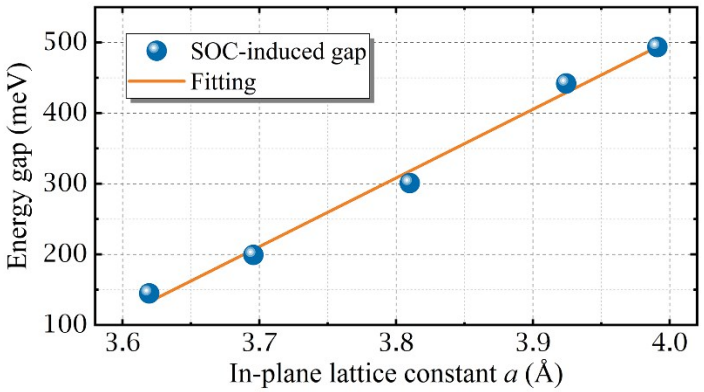

Figure S5. The SOC-induced energy gap of the 2D Fe_2I_2 crystal as a function of biaxial strain effect.

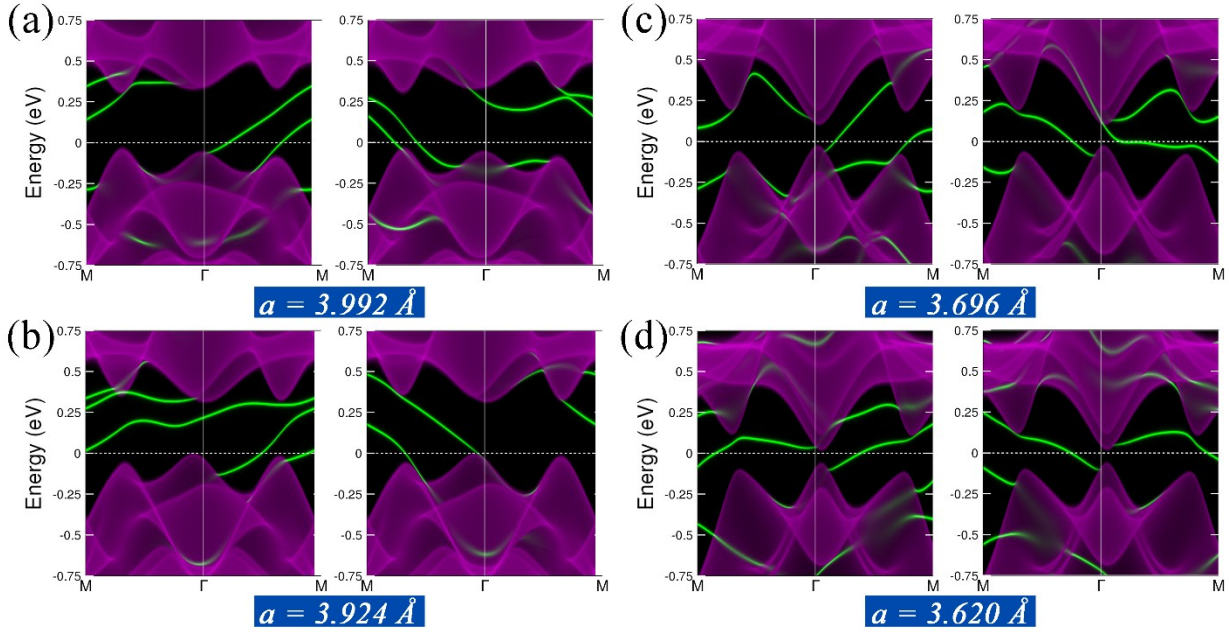

Figure S6. Band structure of the edges of Fe_2I_2 ribbon as a function of in-plane lattice constants (a) 3.992 Å (4.65%), (b) 3.924 Å (3%), (c) 3.696 Å (-3%) and (d) 3.620 Å (-5%) with robust edge states, denoted by green, connecting the 2D valence and conduction bands.

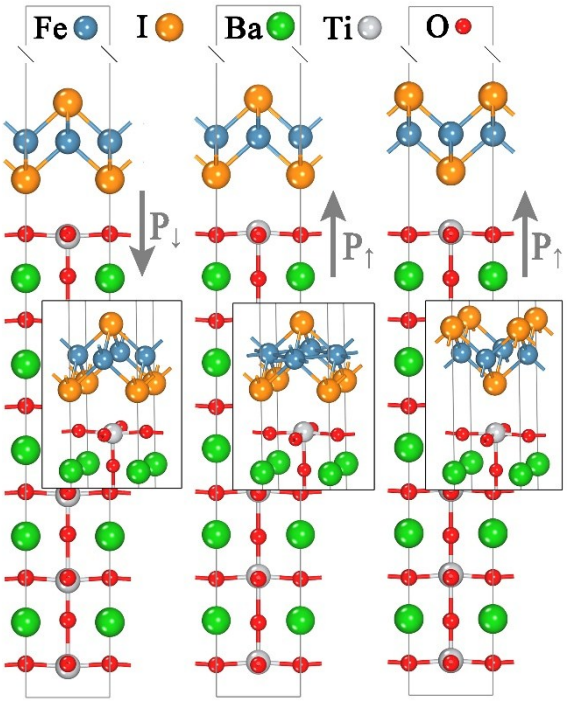

Figure S7. The proposed Fe_2I_2/BTO junctions consisting of Fe_2I_2 SL on five unit cells of $BaTiO_3$. Blue, orange, green, gray and red spheres denote the Fe, I, Ba, Ti, and O atoms, respectively. The gray arrows show the polarization directions.

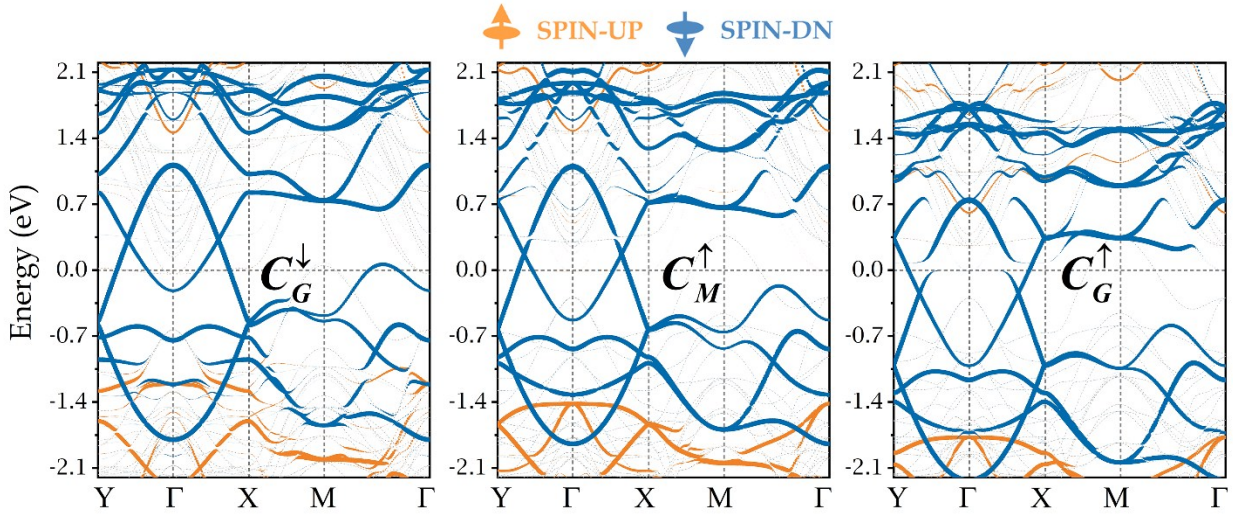

Figure S8. The Fe_2I_2 layer-resolved band structure for the three different Fe_2I_2/BTO configurations, i.e. $C_G^{\downarrow}$ (left panel), $C_M^{\uparrow}$ (central panel), and $C_G^{\uparrow}$ (right panel, respectively).

The SOC energy difference is defined as $\Delta E_{SOC} = (E_{SOC}^{\rightarrow} - E_{SOC}^{\uparrow})/2$, where

$$\Delta E_{SOC} = \frac{\hbar^2}{2m^2c^2}\left\langle \frac{1}{r}\frac{dV}{dr}\hat{L}\cdot\hat{S}\right\rangle$$
$$= \sum_{I,lmm'\sigma\sigma'} \xi_{Il}\left\langle Ilm\sigma\left|\hat{L}\cdot\hat{S}\right|Ilm'\sigma'\right\rangle \rho^{Il}_{mm',\sigma\sigma'}$$

Here, $\rho^{Il}_{mm',\sigma\sigma'} = \frac{1}{N_k}\sum_{nk}\langle Ilm'\sigma' | nk\rangle\langle nk | Ilm\sigma\rangle f(\varepsilon_{nk})$, where I is the atomic index, lm are the angular momentum orbitals, σ, σ' is the spin index, ξ_{Il} is the atomic SOC strength obtained from the spherical part of the effective potential, V(r), within the PAW sphere, $\rho^{Il}_{mm',\sigma\sigma'}$ is the density matrix projected on atomic orbitals, $\hat{L}$ and $\hat{S}$ are the orbital and spin operators, respectively.

low-energy effective Hamiltonian:

In the absence of SOC, the 2D Fe_2I_2 SL hosts two pair of Dirac points along the k_x and k_y axes, locating at (±k_0, 0) and (0, ±k_0), respectively. We have constructed the low-energy effective $k\cdot p$ Hamiltonian to describe the Dirac cones, for instance, for the ones denoted as D_1 (D_2) at (k_0, 0) ((0, k_0)). At D_1 (D_2), the two relevant bands forming the Dirac point are labeled as φ_1 and φ_2. Under basis $\Psi = (\varphi_1, \varphi_2)^T$, the Hamiltonian can be expressed as

$$H_{D_1}(p_x, p_y) = p_x\sigma_3 + p_y(\lambda_1\sigma_1 + \lambda_2\sigma_2)$$
$$H_{D_2}(p_x, p_y) = p_y\sigma_3 + p_x(\lambda_1\sigma_1 + \lambda_2\sigma_2)\ , \qquad \textbf{(Eq. S1)}$$

where $\sigma_{1,2,3}$ are the Pauli Matrices and $\lambda_{1,2}$ are real constants.

References:

1. M. A. McGuire, *Crystals*, 2017, **7**, 121.

2. M. Ashton, D. Gluhovic, S. B. Sinnott, J. Guo, D. A. Stewart and R. G. Hennig, *Nano Lett.*, 2017, **17**, 5251−5257.

3. A. S. Botana, and M. R. Norman, *Phys. Rev. Mater.*, 2019, **3**, 044001.